The Semiclassical Theory of Transport in Topological Weyl Semimetals

by Robert McKay

The Ohio State University

April 2018

Undergraduate Honors Thesis Research
Presented in Partial Fulfillment of the Requirements for graduation "with Honors Research Distinction in Physics" in the undergraduate colleges of The Ohio State University

Research Advisor:
Professor Nandini Trivedi
Physics Department

Abstract

Weyl semimetals are three-dimensional analogs of graphene in which electrons move like light with a linear dispersion. Electrons in Weyl semimetals are subject to Berry curvature, which acts as a magnetic field in momentum space. At their Weyl points, Weyl semimetals possess monopoles of Berry curvature with opposite chirality, or monopole charge. Weyl semimetals come in two types: in type-I, the Weyl cones that describe their energy-momentum relation intersect the zero-energy surface at two pairs of points, whereas type-II Weyl semimetals arise when the Weyl cones are tilted beyond a critical angle that results in electron and hole pockets with finite density of states touching at Weyl points. It is the goal of this project to calculate the effects of these Berry monopoles on transport both with and without an external magnetic field for lattice models of a Weyl semimetal.

We investigate the transport behavior of Weyl semimetals using the semiclassical Boltzmann formulation in which the Berry monopoles are included. We find that the tilt of the energy bands in type-II Weyl semimetals impacts transport properties through the interplay of the states closest in energy to the Weyl nodes. Topology transitions can are represented through different pockets from the hole and electron contribution along the nodal energy plane. As the tilt increases from the type-I regime to the type-II regime, the electron and hole pockets merge at the projection of the energy dispersion at $\epsilon = 0$, resulting in an enhanced transport regime. There are also regions of the tilt where the the hole and electron pockets all merge, resulting in a decrease in magnitude of transport without a magnetic field. The thermoelectric transport coefficient, at a fixed temperature, shows the largest change at the tilt angle where the electron and hole Fermi surfaces merge. We find this is due to the distribution of filled energy states interacting with the net Berry curvature of a Weyl semimetal. The non-monotonic behavior as a function of temperature is obtained through thermoelectric transport coefficients' dependency on temperature resulting from two competing effects: (a) an increase in the number of states around the Fermi level involved in anomalous transport; (b) strong temperature dependence of the chemical potential from its $T = 0$ value to sticking at the Weyl nodes. These results can be extended to the behavior of Weyl semimetals in an external magnetic field.

Upon applying the magnetic field, we obtain a rich context for temperature dependence and magnetic field strength. A variety of varied parameters are considered, such as the scattering times and applied fields. We find the equations governing the nonequilibrium distribution provide strong framework of what the scattering times and field dependences do. We also obtain these relations for different Fermi energies to calculate the Nernst effect, for most values of temperature away from $T = 0$, as a change in the number density of electrons.

1 Introduction to Weyl Semimetals and their Properties

Weyl semimetals are a quantum material containing massless states of electrons, known as Weyl fermions [1]. Hermann Weyl first predicted Weyl fermions' theoretical existence in 1929, only to be discovered decades later in quantum materials [1–4]. Weyl fermions recently impacted condensed matter physics through the discovery of type-I and type-II Weyl semimetals [5–12]. At pairs of points in the energy dispersion of a Weyl semimetal, called Weyl points, the relationship becomes approximately conical [1]. The conical Weyl points cause electrons to behave with linear energy dispersion, similar to light, which classifies the Weyl fermion [1]. This is in contrast to a free electron, whose energy dispersion is quadratic in momentum. The types of Weyl cones can be further classified into type-I and type-II. This thesis will include both type-I Weyl semimetals, whose energy bands exhibit right-angle cones to its zero-energy surface, and type-II Weyl semimetals, whose energy bands display a tilt relative to the zero-energy surface (see Figure 1 for clarification) [5–8]. An important effect of the tilted Weyl cones is that energy states will arrange themselves differently.

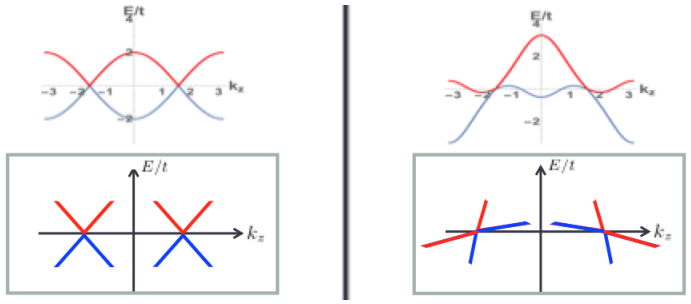

Figure 1: On the left are the energy dispersions for a type-I Weyl semimetal while an example of a type-II Weyl semimeal is on the right. The bottom figures illustrate the cone-like structures in the band energy.

A number of materials exhibit properties that are consistent with Weyl semimetals. TaAs is among one of the first elements to be discovered as a Weyl semimetal [13]. Additionally, $MoTe_2$ is one of the first elements to display strong characteristics of a type-II Weyl semimetal [14]. $WTe_{1.98}$ exhibits a chiral anomaly and WP_2 exhibits thermal transport properties that suggest they may be type-II Weyl semimetals [15, 16]. Additionally, Mn_3Sn and Mn_3Ge have demonstrated anomalous Hall conductivities that are strong indicatives of a time-reversal breaking Weyl semimetal [17–19]. It has also been proposed that one can tune between a type-I and type-II Weyl semimetal through strain [20]. This motivates the work done throughout this thesis.

The Hamiltonian for the model used in the rest of the paper is [21, 22]:

$$\hat{H} = \gamma(\cos(k_z a) - \cos(k_0 a))\hat{\sigma}_0 - 2t\sin(k_x a)\hat{\sigma}_1 - 2t\sin(k_y a)\hat{\sigma}_2 - \Big[2t_z\big(\cos(k_z a) - \cos(k_0 a)\big) + m(2 - \cos(k_x a) - \cos(k_y a)) + \gamma(\cos(3k_z a) - \cos(3k_0 a))\Big]\hat{\sigma}_3 \quad (1)$$

where $\hat{\sigma}_i$ is the i-th Pauli matrix. Equation (1) is derived from the tight binding approach, which allows Weyl fermions to hop to its nearest neighbor potential site. Equation (1) provides control over the degree of tilt of the Weyl cones through the factor γ [22]. The Hamiltonian is a time-reversal breaking model, meaning the Hamiltonian breaks the invariance of time symmetry [21, 22]. Equation (1) was used rather than a continuum cone model, $\hat{H} = \gamma k_z \hat{\sigma}_0 + \chi \hbar v_F(\mathbf{k} - \mathbf{k_0}) \cdot \sigma$, since a continuum model would lead to the unphysical property of open energy states along the energy dispersion's $\epsilon = 0$ plane in the type-II case [21, 22].

A significant effect in Weyl semimetals is Berry curvature. Berry curvature is a quantum mechanical effect that contributes an overall phase to an electron's wave function [23, 24]. Berry curvature can be thought of as $\mathbf{\Omega} = \nabla_{\mathbf{k}} \times \mathbf{A}$ where $\mathbf{A}$ is the Berry vector potential. The Berry vector potential is defined as $\mathbf{A} = i\psi^* \nabla_{\mathbf{k}} \psi$ where ψ is a wave state. This definition of the Berry vector potential comes out of considering the geometric contribution from a phase. Although an overall phase does not affect the energy of the electron, it will influence its trajectory through momentum space. This consideration and geometric impact comes from the topology in the Brillouin zone. In fact, the Berry field can be viewed as behaving like a magnetic field in momentum space. The magnetic field parallels the Berry curvature in that both are defined as curls of a vector potential. In addition, the overall geometric phase, γ, that a wave state will pick up from Berry curvature is the flux through a closed surface in k space, $\gamma = \oint_s \mathbf{\Omega} \cdot d^2\mathbf{k}$, which parallels the flux of a magnetic field in real space $\oint_s \mathbf{B} \cdot d^2\mathbf{r}$ [25]. This becomes further apparent when the equations of motion are considered. The expression for velocity of the n-th band is [26]:

$$\dot{\mathbf{r}}_n = \mathbf{v}_n(\mathbf{k}) - \big(\dot{\mathbf{k}} \times \mathbf{\Omega}_n(\mathbf{k})\big) = \frac{1}{\hbar}\nabla_{\mathbf{k}} \mathcal{E}_n(\mathbf{k}) - \big(\dot{\mathbf{k}} \times \mathbf{\Omega}_n(\mathbf{k})\big) \quad (2)$$

,

and the expression for the Lorentz force is:

$$\dot{\mathbf{k}} = q\mathbf{E} + q\dot{\mathbf{r}}_n \times \mathbf{B} \quad (3)$$

. The $\dot{\mathbf{k}} \times \mathbf{\Omega}_n(\mathbf{k})$ is what leads to curving behavior in the electron trajectories. Through some vector calculus

manipulations, Equation (2) and (3) can be expressed as uncoupled equations [26]:

$$\dot{\mathbf{r}}_n = \frac{\mathbf{v}_n + \frac{q}{\hbar}\mathbf{E} \times \mathbf{\Omega}_n + \frac{q}{\hbar}(\mathbf{v}_n \cdot \mathbf{\Omega}_n)\mathbf{B}}{1 - \frac{q}{\hbar}\mathbf{B} \cdot \mathbf{\Omega}_n} \tag{4}$$

$$\dot{\mathbf{k}} = \frac{q\mathbf{E} + \frac{q}{\hbar}(\mathbf{v}_n \times \mathbf{B}) + \frac{q^2}{\hbar}(\mathbf{E} \cdot \mathbf{B})\mathbf{\Omega}_n}{1 - \frac{q}{\hbar}\mathbf{B} \cdot \mathbf{\Omega}_n} \tag{5}$$

The equation of Berry curvature from a wavefunction of a tight binding model is given as [24]:

$$\Omega_i(\mathbf{k}) = \epsilon_{ijl}\frac{\mathbf{d} \cdot (\partial_{k_j}\mathbf{d} \times \partial_{k_l}\mathbf{d})}{2|\mathbf{d}|^3} \tag{6}$$

Where $\mathbf{d}$ is defined such that $\hat{H} = \sigma \cdot \mathbf{d}$ and σ is a vector composed of the Pauli matrices from Equation (1). Equation (6) can be used to find the Berry curvature around each of the Weyl nodes. This expression can be approximated by the continuum case of $\Omega_i(\mathbf{k}) = \chi_i \frac{\mathbf{k}}{2k^3}$, which is a monopole of chirality, or monopole charge, χ_i [27–30]. However, we are not using the continuum case, so the actually expression is a bit more complicated, but the monopole result is still correct around the Weyl nodes. This expression can be compared to Equation (1) to find the values of $\mathbf{d}$ from Equation (1). This means that a Weyl semimetal exhibits magnetic monopole properties as it directs the Weyl fermion's deflection as it travels [27–33]. This will become important when considering how the altered trajectories influence transport.

2 Introduction to Transport

We will consider the transport of charge and heat, or electric current and heat current respectively, in this thesis. These Onsager transport equations are compactly written with the following tensorial relation [34]:

$$\begin{pmatrix} \mathbf{J}^e \\ \mathbf{J}^q \end{pmatrix} = \begin{pmatrix} \mathbf{L}^{EE} & \mathbf{L}^{ET} \\ \mathbf{L}^{TE} & \mathbf{L}^{TT} \end{pmatrix} \cdot \begin{pmatrix} \mathbf{E} \\ -\nabla T \end{pmatrix} \tag{7}$$

For electric current, $\mathbf{J}^e$, one can apply an electric field, $\mathbf{E}$, and look at the linear response in the in the parallel or transverse direction, $\mathbf{L}^{EE}$. Similarly, one can apply a temperature gradient, $-\nabla T$, and calculate the heat current, $\mathbf{J}^q$, from the linear response term, $\mathbf{L}^{TT}$. However, cross responses are also considered, such as applying a temperature gradient and obtaining an electric current from $\mathbf{L}^{ET}$ or applying an electric field and obtaining a heat current from $\mathbf{L}^{TE}$. However, due to symmetries, $\mathbf{L}^{ET}$ and $\mathbf{L}^{TE}$ are related by a temperature T through $\mathbf{L}^{ET} = T\mathbf{L}^{TE}$, so only one of these coefficients needs to be considered [34]. It

is important to note that these response terms are tensors. Conductivity is the response from an electric field while the thermoelectric coefficient details such a response from a thermal gradient. Also, the thermal conductivity provides a response in thermal current from a temperature gradient. We also inspect the Seebeck effect and Nernst effect, which details the response in an electric field from an applied magnetic field and temperature gradient in orthogonal directions [35]. The Seebeck effect is [35, 36]

$$\alpha_{xxz} = \frac{E_x}{-\nabla_x T} = \frac{-L_{xx}^{ET} L_{xx}^{EE} + L_{xy}^{ET} L_{xy}^{EE}}{(L_{xx}^{EE})^2 + (L_{xy}^{EE})^2} \tag{8}$$

and the Nernst effect is given by [35, 36]

$$\alpha_{xyz} = \frac{E_y}{-\nabla_x T} = \frac{L_{xx}^{EE} L_{xy}^{ET} - L_{xy}^{EE} L_{xx}^{ET}}{(L_{xx}^{EE})^2 + (L_{xy}^{EE})^2} \tag{9}$$

Here, the index of α_{ijk} represents a temperature gradient in the i-direction, an electric field response in the j-direction, and a magnetic field in the k-direction. The Seebeck effect is when the response is in the same direction as the applied temperature gradient whereas the Nernst effect is the response in the transverse direction to the temperature gradient.

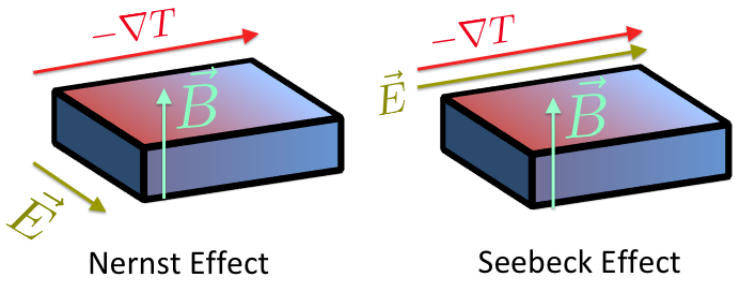

Figure 2: The Nernst effect is on the left, with a temperature gradient, $-\nabla T$, an electric field $\mathbf{E}$, and an applied magnetic field $\mathbf{B}$. The right illustrates the Seebeck effect.

Equations (8) and (9) can be derived from Equation (7) by allowing the current terms to reach an equilibrium at 0 [26, 35, 36].

Explicit forms for these coefficients are found using the semiclassical Boltzmann formalism. This formalism lets us incorporate the following equations of transport at nonequilibrium energy distributions [21, 37–41]:

$$\begin{aligned} \mathbf{J}^e = &- e \int \frac{d^3\mathbf{k}}{(2\pi)^3} (\mathbf{v} + \frac{e}{\hbar}\mathbf{E} \times \mathbf{\Omega}) f \\ &+ \frac{\nabla T}{T} \times (\frac{e}{\hbar} \int \frac{d^3\mathbf{k}}{(2\pi)^3} \mathbf{\Omega}[(\epsilon - \mu) f_0 + k_B T \ln(1 + e^{-\beta(\epsilon-\mu)})]) \end{aligned} \tag{10}$$

$$\mathbf{J}^q = \int \frac{d^3\mathbf{k}}{(2\pi)^3}(\epsilon-\mu)\mathbf{v}f$$
$$+ \int \frac{d^3\mathbf{k}}{(2\pi)^3}(\mathbf{E}\times\frac{e}{\hbar}\mathbf{\Omega}\{(\epsilon-\mu)f_0 + k_BT\ln 1 + e^{-\beta(\epsilon-\mu)}\}) \tag{11}$$
$$+ \frac{ek_B\nabla T}{\beta\hbar}\times\int\frac{d^3\mathbf{k}}{(2\pi)^3}\mathbf{\Omega}[\frac{\pi^2}{3} + f_0\ln^2(1/f_0-1) - \ln^2(1-f_0) - 2\mathrm{Li}_2(1-f_0)]$$

Here, the group velocity of the electron, $\mathbf{v}$, is $\nabla_{\mathbf{k}}\epsilon$, μ is the chemical potential for a given temperature, $\beta = \frac{1}{k_BT}$ for temperature T, $\mathbf{\Omega}$ is the Berry field, and $\mathrm{Li}_n(z) = \sum_{k=1}^{\infty}\frac{z^k}{k^n}$. Also, f_0 represents the equilibrium Fermi distribution from statistical mechanics, but f represents the distribution of fermion energy states for nonequilibrium distribution (i.e. when an electric field, magnetic field, or temperature gradient is applied). Liouville's theorem tells us that the volume in phase space of a partition function is incompressible, so it follows the nonequilibrium Boltzmann distribution is solved by realizing that applying fields and gradients only shifts the partition function in phase space [37]. Since the basic partition function represents a discrete volume in phase space, then a displacing field shifts the partition and, hence, will shift f. This relationship can be summarized by this steady-state Boltzmann equation [26, 37, 40, 41]:

$$\frac{d}{dt}f = (\frac{\partial}{\partial t} + \dot{\mathbf{r}}\cdot\nabla_{\mathbf{r}} + \dot{\mathbf{k}}\cdot\nabla_{\mathbf{k}})f = -\frac{f-f_0}{\tau} \tag{12}$$

Equation (12) can be thought of as a multivariable expansion of the continuity equation with a relaxation-time approximation ($\frac{f-f_0}{\tau}$) [37, 40]. The above also includes the average time between scattering events to be τ.

Now with a magnetic field impacting the nonequilibrium Boltzmann distribution given in Equation (12), the Equations (10) and (11) will lead to new terms in addition to the previously described anomalous terms. Upon solving for the nonequilibrium distribution one can find a relation for the resulting transport coefficients (from the tensors of Equation (7)). Before these equations are considered, we will first define the following relations [40]:

$$c_x = eBD\frac{[\frac{v_x}{m_{xy}} - \frac{v_y}{m_{xx}}][-\frac{eBv_y}{m_{xx}} + \frac{eBv_x}{m_{xy}} - \frac{v_x}{D\tau}] + [\frac{v_x}{m_{yy}} + \frac{v_y}{m_{xy}}][-\frac{eBv_y}{m_{xy}} + \frac{eBv_x}{m_{yy}} - \frac{v_y}{D\tau}]}{[-\frac{eBv_y}{m_{xx}} + \frac{eBv_x}{m_{xy}} - \frac{v_x}{D\tau}]^2 + [-\frac{eBv_y}{m_{xy}} + \frac{eBv_x}{m_{yy}} - \frac{v_y}{D\tau}]^2} \tag{13}$$

$$c_y = eBD\frac{[\frac{v_x}{m_{xy}} - \frac{v_y}{m_{xx}}][-\frac{eBv_y}{m_{xy}} + \frac{eBv_x}{m_{yy}} - \frac{v_y}{D\tau}] - [\frac{v_x}{m_{yy}} + \frac{v_y}{m_{xy}}][-\frac{eBv_y}{m_{xx}} + \frac{eBv_x}{m_{xy}} - \frac{v_x}{D\tau}]}{[-\frac{eBv_y}{m_{xx}} + \frac{eBv_x}{m_{xy}} - \frac{v_x}{D\tau}]^2 + [-\frac{eBv_y}{m_{xy}} + \frac{eBv_x}{m_{yy}} - \frac{v_y}{D\tau}]^2} \tag{14}$$

Where $D = (1 + \frac{e}{\hbar}\mathbf{B}\cdot\mathbf{\Omega})^{-1}$ is a coupling term of the magnetic field and the Berry field that arises from Equations (4) and (5) when $r(t)$ and $k(t)$ are uncoupled [40]. Additionally, the terms that go as m_{ij} are

components of the effective mass tensor, which defines an effective mass in the tight binding model [42]. It is more convenient to consider an effective mass when considering why a given fermion has a non-quadratic energy dispersion in the presence of a periodic potential system [42]. The inverse effective mass is defined as $m_{ij}^{-1} = \frac{1}{\hbar^2}\frac{\partial^2}{\partial k_i \partial k_j}\epsilon$ [42]. So an entry in the effective mass tensor m_{ij} is just an entry from the inverse of tensor composed of m_{ij}^{-1}. We will now express the transport coefficients at a nonzero magnetic field, using Equations (13) and (14):

The conductivities [40, 43]:

$$L_{xx}^{EE} = \frac{e^2}{\hbar}\int \frac{d^3\mathbf{k}}{(2\pi)^3} v_x^2 \tau(-\frac{\partial f_0}{\partial \epsilon})(c_x - D) \tag{15}$$

$$L_{xy}^{EE} = \frac{e^2}{\hbar}\int \frac{d^3\mathbf{k}}{(2\pi)^3} [v_y^2 c_y + v_x v_y (c_x - D)]\tau(-\frac{\partial f_0}{\partial \epsilon}) + \frac{e^2}{\hbar}\int \frac{d^3\mathbf{k}}{(2\pi)^3}\Omega_z f_0 \tag{16}$$

The transverse thermoelectric coefficients [40, 41, 43]:

$$L_{xx}^{ET} = \frac{k_B e}{\hbar}\int \frac{d^3\mathbf{k}}{(2\pi)^3} v_x^2 \tau \frac{\epsilon - \mu}{T}(-\frac{\partial f_0}{\partial \epsilon})(c_x - D) \tag{17}$$

$$L_{xy}^{ET} = \frac{k_B e}{\hbar}\int \frac{d^3\mathbf{k}}{(2\pi)^3} [v_y^2 c_y + v_x v_y (c_x - D)]\tau \frac{\epsilon - \mu}{T}(-\frac{\partial f_0}{\partial \epsilon}) + \frac{k_B e}{\hbar}\int \frac{d^3\mathbf{k}}{(2\pi)^3}\Omega_z s_k \tag{18}$$

Where $s_k = -f_0 \ln f_0 - (1 - f_0)\ln(1 - f_0)$ is the entropy density function. The thermal conductivities [40, 43, 44]:

$$L_{xx}^{TT} = \frac{k_B^2}{\hbar}\int \frac{d^3\mathbf{k}}{(2\pi)^3} v_x^2 \tau \frac{(\epsilon - \mu)^2}{T}(-\frac{\partial f_0}{\partial \epsilon})(c_x - D) \tag{19}$$

$$\begin{aligned} L_{xy}^{TT} =& \frac{k_B^2}{\hbar}\int \frac{d^3\mathbf{k}}{(2\pi)^3} [v_y^2 c_y + v_x v_y (c_x - D)]\tau \frac{(\epsilon - \mu)^2}{T}(-\frac{\partial f_0}{\partial \epsilon}) \\ &+ \frac{k_B^2 T}{\hbar}\int \frac{d^3\mathbf{k}}{(2\pi)^3}\Omega_z g_k \end{aligned} \tag{20}$$

Where we define $g_k = [\frac{\pi^2}{3} + f_0 \ln^2(1/f_0 - 1) - \ln^2(1 - f_0) - 2\mathrm{Li}_2(1 - f_0)]$ [44]. Returning to Equations (16), (18), and (20), we will focus on the transverse terms that still exist without an applied magnetic field. This is known as anomalous transport, since transverse transport is achieved without the need of an external magnetic field [21, 40, 43, 45, 46]:

$$L^{EE}_{xy,\text{ anomalous}} = \frac{e^2}{\hbar}\int \frac{d^3\mathbf{k}}{(2\pi)^3}\Omega_z f_0 \tag{21}$$

$$L^{ET}_{xy,\text{ anomalous}} = \frac{k_B e}{\hbar}\int \frac{d^3\mathbf{k}}{(2\pi)^3}\Omega_z s_k \tag{22}$$

$$L^{TT}_{xy,\text{ anomalous}} = \frac{k_B^2 T}{\hbar}\int \frac{d^3\mathbf{k}}{(2\pi)^3}\Omega_z g_k \tag{23}$$

These anomalous transport coefficients are the focus of Section 3 while the generalized transport equations with a magnetic field are the subject of Section 4.

3 Weyl Fermion Trajectories

This section analyzes the motion of a Weyl fermion in a variety of field configurations. The main purpose of this section is to provide motivation as to why transport is interesting in a Weyl semimetal. To do so, we will solve for the equations of motion given in Equation (4) and (5). The typical equations of motion in Equations (2) and (3) now have Berry curvature to them, such as the anomalous velocity term, $-\left(\dot{\mathbf{k}}\times\mathbf{\Omega}_n(\mathbf{k})\right)$, which will affect the motion of the fermion. The trajectories will show how Berry curvature acts like a magnetic field, leading to transverse motion to an applied electric field. To be consistent throughout these calculations, we have chosen the initial momentums in k_x, k_y, and k_z directions to all be $0.01\hbar/a$ in all cases, and the initial location to start at the origin in real space. Furthermore, the applied electric field will always be $0.1t/(ae)$ in the $\hat{x}$.

3.1 Free Particle Gas Comparison to the Weyl Fermion with a Magnetic Field

Before considering the equations of motion of a Weyl semimetal, we will consider the well-known case of a free particle gas with quadratic energy dispersion. The free particle gas has energy dispersion $\epsilon = \frac{\hbar^2 k^2}{2m}$, and we let the electric field be in the $\hat{x}$-direction with magnitude $0.1\frac{ea^2}{\hbar}$ and the magnetic field in the $\hat{z}$-direction. The free particle gas has energy dispersion $\epsilon = \frac{\hbar^2 k^2}{2m}$, and we let the electric field in the $\hat{x}$-direction and the magnetic field in the $\hat{z}$-direction. Unless otherwise specified, we will turn off the Berry interaction do that $\mathbf{\Omega} = \mathbf{0}$ for comparative purposes. The equations of motion, when solved, yield:

$$\ddot{k}_y = -\frac{e^2 B}{m\hbar}E - \frac{e^2 B^2}{m^2}k_y \tag{24}$$

$$k_x = \frac{m}{eB}\dot{k}_y \tag{25}$$

$$k_z = k_{z0} \tag{26}$$

$$\dot{r} = \frac{\hbar}{m}\begin{bmatrix} k_x \\ k_y \\ k_z \end{bmatrix} \tag{27}$$

These trajectories produce what we would expect: Equation (24)'s solution follows $A\cos(\omega t + \delta)$ with an additional constant solution from E, so Equation (25)'s solutions must also be trigonometric and the x and y entries in Equation (27) must also be periodic to a sine or cosine term. The purpose of this is to show how a Weyl semimetal's band structure differs from a free particle gas and how the Berry curvature manifests this difference. The classical free particle gas results from Equations (24) to (27) are illustrated in Figure 4. This provides the well-known results described by Maxwell: the electric field furnishes a continuous momentum contribution, increasing the linear velocity of the electron, whereas, the magnetic field provides orthogonal changes in the velocity in real space, resulting in an orbital path. The periodicity and phase change between momentum and real space follow intuition, as the electron will change direction according to its instantaneous velocity at any point. It is important to note both the momentum $\hbar\mathbf{k}$ and the spatial trajectory $\mathbf{r}$ are altered by the magnetic field.

We now consider a Weyl fermion. For simplicity, we will confine the Weyl fermion to the type-I Weyl semimetal model in which $\gamma = 0$ and let the other parameters be $m = 3t$, $t_z = t$, $k_0 a = \pi/2$ in the model described by Equation (1). We keep the same initial momentum and electric field of the free particle gas. The only difference is the applied magnetic field is half of its strength in the free particle gas case, to better illustrate finer features. The resulting trajectories are illustrated in Figure 5. We compare these results to the free particle gas in magnetic and electric fields in Figure 4 to draw attention to the difference between the Weyl fermion and the free fermion. Because $\mathbf{v}_k = \frac{1}{\hbar}\nabla_{\mathbf{k}}\epsilon$, the velocities as a function of $\mathbf{k}$ are now some combination of sines and cosines. Unlike the free particle gas case, each component of the velocity, $x(t)$, $y(t)$, and $z(t)$, will have a dependence on all of k_x, k_y, and k_z. This traces back to the term in Equation (2), which has a dependence on the $\nabla_k\epsilon(k_x, k_y, k_z)$. Since ϵ will depend on k_x, k_y, and k_z due to the determinant of the Hamiltonian from Equation (1). Hence, if any of these components couples with a field, it will influence all of the $\mathbf{v}_k$ components. Due to crossing periodic potential wells in the lattice structure, the Weyl fermion exhibits periodic trajectories, known as Bloch oscillations, in Figure 5(a-b). The momentum trajectories

follow expected paths in a constant electric field with no magnetic field: constant in the initial conditions and linear with time in the direction of **E**. The result of this is that when the magnetic field is also turned on, the momentum terms become similar to the free particle gas. Take the example of Figures 4(g) and 5(g). The electric field supplies the same motion, $k_x = eEt + k_{x0}$ by Equation (3). When the magnetic field is supplied, the equation of motion still goes as Equation (25) but now as $\dot{k}_y = \frac{eB}{m}\frac{\partial \epsilon}{\partial k_x}$. Since ϵ is dependent on all of k_x, k_y, k_z, then the simple linear relation does not hold anymore. However, the other influences are periodic and small, so they will approximately resemble each other.

Furthermore, all the plots in the central column of (b, e, h, k) closely match in the free fermion case and the Weyl fermion case. The difference lies in the Bloch oscillations of the Weyl semimetal causing the magnetic deviations of trajectories to oscillate in its path. For example, Figure 5(e) displays beveled oscillations while the corresponding free particle gas in Figure 4(e) shows elongated oscillations with flatter peaks. It is reasonable to say the magnetic field can reinforce the hopping between sites for the fermion. The assist from the magnetic field let the electron make more aggressive hops, going to $\approx 250a$ in the $\hat{y}$-direction in the same time it takes the free electron to go $\approx 120a$. The difference in these types of oscillations is in how the magnetic field provides acceleration along a path that runs into periodic potentials from the lattice. Figure 5(e) tells us the electron stays in a higher velocity regime for a longer time, compared to Figure 4(e).

Another stark difference is at the velocity, $\dot{z}(t)$, in Figure 5(f). Even without the magnetic field, the motion still undergoes Bloch oscillations due to its dependence on k_x and k_y, which do change with the magnetic field. From the mixing of k_x and k_z, there exists a deviation from the electric field trajectory due to this intricate interplay of momentums in the Hamiltonian. However, the time scale by which they deviate becomes the strongest at around $10\hbar/t$, which the magnetic field interplaying with the band structure curves away from the electric field the most. There is now a pair of oscillators that have different periods and amplitudes from Figure 5(g) and (h) that interfere to produce the motion in Figure 5(f) and 5(c). In the free particle gas case, the dependence on momentum is more straightforward in Equation (26) and easy to see why the magnetic field has no deviation since the curl operator does not allow a magnetic field to couple with a velocity component in the same direction. Some differences exist in the (a) and (d) sections of these two figures. Particularly, the unconstrained quadratic nature of the free particle gas model manifests itself in Figure 4(a) and (d), for the electric field accelerates this particle in the $\hat{x}$-direction while the magnetic field adds cyclic motion to $x(t)$ and $\dot{x}(t)$. Conversely, the Weyl fermion is constrained to periodic potentials that restrict the acceleration to Bloch motion, shown in Figure 5(a) and (d). The result is the path still exhibits periodic motion while the magnetic field offers a deviation to this motion.

3.2 Comparison of a Magnetic Field to a Berry Field Acting on a Weyl Fermion

We now contrast the Weyl fermion subject to a magnetic field interaction to that subject to the Berry curvature interaction. We will maintain the same parameter choice as the previous subsection. As mentioned in the introduction, Berry field acts like a magnetic field in momentum space and parallels the Lorentz law. The Berry field we will use will be from Equation (6), which results in two monopoles of opposite chirality along the $\hat{k}_z$ and separated by k_0 from the Hamiltonian in Equation (1). The trajectories with electric field and Berry field are given in Figure 6. One can identify a variety of differences. First, the magnetic field in momentum space produced some type of orbital in Figure 5(g-h), whereas the Berry curvature leaves the momentum space linear in time and unaffected by the Berry interaction in Figure 6(g-h). This is due to the Lorentz force from Equation (3), which now only experiences a boost from the electric field since $B = 0$. Comparing the $y(t)$ trajectories in Figure 5(b) and Figure 6(b), the Berry curvature plot diverges in increments away from the path without Berry curvature, whereas the magnetic field case shows a nonincremental divergence from the electric field induced path. This difference is the result of of the Berry field expressing periodic monopoles, so that as the fermion travels between a nodal pair, along the k_z axis in momentum space, the Berry curvature is strongest and provides a strong deviating velocity and then weakens this deviation as the fermion gets farther from the nodal pair. Conversely, the fermion in Figure 5(b) experiences a constant magnetic field, so its deviation from the **E** path is more linear in time.

Additionally, examining the corresponding velocity components from the magnetic field case (Figures 5(d-f)) and Berry field case (Figures 6(d-f)), the magnetic field produces sinusoidal differences in the velocity. However, although the trajectory for the Berry curvature situation also has some periodicity to it, the function is more sharply peaked as it grows and dies rapidly. This is attributed to passing between two opposite monopoles through space. Additionally, the Berry curvature only produces a $\hat{y}$ component in Figure 6(e) since the sum of the Berry curvature in only in the $\hat{z}$-direction and only couples to the time dependent k_x term. This contrasts the sinusoidal velocity terms from the magnetic field case in Figure 5(d-f).

Thus, Weyl semimetals' remarkable property of Berry monopoles exhibit distinctive consequences: the sharper divergences are possible through this monopolist behavior. If one applies an electric field through a Weyl semimetal, transverse velocity of the charged fermion is expected. Hence, in motivation of the next two sections, Berry curvature exhibits peculiar behavior in Weyl semimetals, which leads to significant Weyl trajectories. This suggests the transport of charge and thermal energy will also be distinctive. In the next two sections, we will explore the consequences of the Weyl semimetal model on transport properties.

4 Transport Without an External Magnetic Field

We will now examine the role that the Berry curvature plays in anomalous transport. With this model, we will first consider adjusting the tilt from the type-I Weyl semimetal to the type-II Weyl semimetal. We will investigate the electric current response in the transverse direction from the conductivity, known as the Hall coefficient, and the transverse thermoelectric coefficient. Additionally, we will examine the thermal current response from a transverse temperature gradient. Another focus of these anomalous terms will be how the temperature dependence affects the transport.

4.1 Anomalous Transport vs. Tilt

The model described in equation (1) allows for Lifshitz transitions [47]. These transitions can be viewed along the ϵ=0 plane of the energy dispersion, where, at critical values of the tilt, pockets of states will either form or merge [21, 47]. The regions between Lifshitz transitions are displayed in Figure 7(e-h). The energy configuration starts out in the type-I regime of low γ, where just a pair of points in the intersection is obtained. However, as γ is increased, these points grow into two regions of pockets: one from the electron contribution and one from the hole contribution. The next Lifshitz transition emerges at the instance when the electron pockets fuse at $\gamma \approx 2t$. The last Lifshitz transition occurs once the hole pocket merges near $\gamma \approx 2.5t$. These transitions are important in relating what configuration of momentum is available closest to the Weyl nodes, where Berry curvature is strongest. This consideration will become important when considering the anomalous Hall coefficient, transverse thermoelectric coefficient, and thermal coefficient.

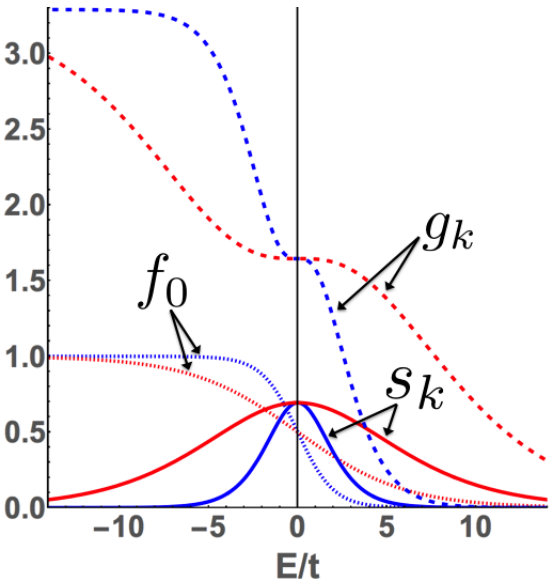

Figure 3: This figure illustrates the integration kernels of $L^{EE}_{xy,\text{ anomalous}}$, $L^{ET}_{xy,\text{ anomalous}}$, and $L^{TT}_{xy,\text{ anomalous}}$, corresponding to f_0, s_k, and g_k, respectively. This is plotted for $\mu = 0$ and temperatures $T = 1t/k_B$ (blue) and $T = 3t/k_B$ (red).

The anomalous Hall, transverse thermoelectric, and traverse thermal coefficients from Equations (21), (22), and (23) are plotted as functions of the tilt in Figure 10(a-c). $L^{ET}_{xy,\text{ anomalous}}$ displays distinct regions of tilt. From the type-I regime of $\gamma = 0$ to $\gamma = 0.5t$, a small enhancement of the anomalous ther-

moelectric coefficient occurs. This is due to the interplay between the nodal tilt, the connectivity of the Fermi pockets, and the temperature dependence of the chemical potential. One tool to understanding this interplay is what is called net Berry curvature, which is the Berry curvature integrated across surfaces of constant energy dispersion in the Brillouin zone. In the $\hat{z}$-direction, this is given by:

$$\Omega_z^{\text{net}}(\epsilon) = \sum_n \int \frac{d\mathbf{S}}{(2\pi)^3} \frac{\Omega_{n,z}(\mathbf{k})}{|\nabla_{\mathbf{k}}\epsilon|} \tag{28}$$

where the index n sums over the different Berry fields due to the various band energies, and $\mathbf{S}$ is the differential surface at a shell of constant energy. The net Berry curvature for each Lifshitz transition is plotted in Figure 9(a-d). The net Berry curvature is odd at $\gamma \sim 0$, so equal and opposite contributions in the positive and negative energies yield little enhancement in the anomalous thermoelectric transport. However, upon hitting the first Lifshitz transition at $\gamma \approx 0.5t$, where the two pockets initially emerge, the net Berry curvature now has a peak to it, with unequal contributions from the positive and negative energies. The result of this is an enhancement in the magnitude of $L^{ET}_{xy,\text{ anomalous}}$, shown in Figure 10(b). Between the next two Lifshitz transitions of $2t \lesssim \gamma \lesssim 2.5t$, the net Berry curvature reaches its deepest peak value, with the result of this being $L^{ET}_{xy,\text{ anomalous}}$ also reaches its peak value. After the final Lifshitz transition region where the hole and electron pockets are both merged at $\gamma \gtrsim 2.5t$, a decrease in the magnitude of $L^{ET}_{xy,\text{ anomalous}}$ is present, which matches to the lesser-in-magnitude net Berry curvature with a now less well-defined peak. To summarize, the anomalous thermoelectric coefficient plotted against the tilt parameter leads to distinct regions between the Lifshitz transition that are sensitive to Berry curvature.

The anomalous Hall coefficient, $L^{EE}_{xy,\text{ anomalous}}$, in Figure 10(a) offers similar features. The same properties dictating the net Berry curvature at various tilt regions still apply. However, the main difference is the integrand kernel from Equation (21) now involves the Fermi distribution function, which quickly flattens out for higher temperatures. In addition, the density of states around the nodes is also where the Berry curvature is strongest, resulting in a rich correspondence between the Berry curvature and the energy states occupied from the chemical potential. Hence, the Fermi distribution kernel will dictate how the Berry curvature interplays with the occupied energy states.

Similarly, the same guiding effects as $L^{EE}_{xy,\text{ anomalous}}$ and $L^{ET}_{xy,\text{ anomalous}}$ apply to $L^{TT}_{xy,\text{ anomalous}}$ from Figure 10(c). Much like the previous two transport coefficients, the net Berry curvature plays the same role among the same regions of the tilt. However, the integration kernel, from Equation (23), now has a broader inflection point around the chemical potential than does the Fermi distribution function. The result of this is that $L^{TT}_{xy,\text{ anomalous}}$ is more sensitive to Berry curvature over a wider range of energies than $L^{EE}_{xy,\text{ anomalous}}$. This manifests in the transport making a decrease in magnitude around the tilt where the electron pockets first

merge. In addition, this kernel is more sensitive to the changing chemical potential and nodal crossing, which is evident in the enhancement of the anomalous thermal coefficient with increasing temperatures. Hence, the broader kernel of integration impacts the sensitivity of the transport equations.

4.2 Anomalous Transport for a Variety of Fermi Energies

Before considering the effect of changing the Fermi energy, ϵ_f, on the anomalous transport coefficients as a function of temperature, the effect of changing the chemical potential with the Fermi energy must first be explored, shown in Figure 9(i-l). However, we will first examine some guiding models to show how chemical potential changes with Fermi energies and interplays with the energy bands. The chemical potential as a function of temperature is determined self-consistently through the electronic number density, where the number density is given by [36, 48]:

$$n = \int_{-\infty}^{\infty} d\epsilon g(\epsilon) f_0(\epsilon, \mu) \tag{29}$$

The number density is set at $T = 0$ by ϵ_F, the maximum energy at this temperature. Since number density should not change as temperature increases, the number density must also be the same for any nonzero temperature, so the chemical potential can be determined at any temperature by self-consistently solving for $\mu(T)$ for fixed n. Plots of the quadratic energy dispersion $\epsilon = \frac{\hbar^2 k^2}{2m}$ and of the single band cosine energy dispersion $\epsilon = -2t(\cos(k_x a) + \cos(k_y a) + \cos(k_z a)) + 6t$ are given in Figure 8(a) and (b). For the cosine band, this describes a cubic lattice of real spacing a and energy hopping parameter t. Since the ϵ_F's are low enough, the cosine band will give similar results for the number density n. We see that a single band yields unrestrained chemical potential with increasing temperature. The changing ϵ_F just alters where μ intercepts at $T = 0$. However, when we add a secondary band, $\epsilon = \pm(-2t(\cos(k_x a)+\cos(k_y a)+\cos(k_z a))+6t)$, in Figure 8(c), this puts a restraint on the chemical potential and provides negative contribution from the lower band energies. The result is that as more energies become accessible with increasing temperature, the negative and positive bands provide opposite contributions, such that the chemical potential now approaches a constant offset value with increasing T which is set by ϵ_F. This matches with observations that μ is approximately constant with higher values of T.

We will now switch back to considering the dependence of the chemical potential on temperature of the Weyl nodes. By shifting the Fermi energy, the area under the density of states in Figure 9(e-h) is changing and therefore the number density of electrons also changes. The plot of μ is determined by the shape and area of the density of states and the Fermi energy. By including a tilt parameter, the minimum of the density of states is shifted in Figure 9(e-h), so that the chemical potential will cross the nodal energy level

at ϵ=0, shown in Figure 9(j-l). This is opposed to the type-I Weyl semimetal, whose μ approaches the nodal energy asymptotically but never crosses it in Figure 9(i). By increasing the Fermi energy, the point where the chemical potential crosses the nodal energy also increases. This nodal crossing will become pertinent in the context of transport.

By varying the Fermi energies, the number density of electrons at $T = 0$ is also varied. These results are plotted in Figure 10(d-f). The anomalous thermoelectric coefficient (Figure 10(e)), at larger temperatures, experiences an increase in magnitude with increasing Fermi energy. This is because the entropy density function encounters a broad increase with expanding the energies over which $L^{ET}_{xy,\text{ anomalous}}$ is integrated. Another interesting feature is that as Fermi energies go further from the Weyl node, the maximum value of $L^{ET}_{xy,\text{ anomalous}}$'s magnitude also increases. Similarly, when the anomalous Hall coefficient is considered (Figure 10(d)) for a variety of Fermi energies, a general decrease in the enhancement of the absolute value of $L^{EE}_{xy,\text{ anomalous}}$ occurs. This is due to the iteration of the chemical potential over the Fermi energy, which, in general, increases the chemical potential function with temperature. The result of this increase on the Fermi distribution function shifts the integration region of the Hall transport, resulting in a decreased effect. For larger T, these anomalous Hall functions coalesce into a single line; the reasoning is that chemical potential reaches a maximum value so that the Hall coefficient becomes uniform with E_f. Finally, the anomalous thermal coefficient (Figure 10(f)) has nearly negligible differences as the Fermi energy varies. This is due to the kernel of integration broadening to a point and varying the Fermi energy, which is washed out in the integration. These results were only illustrated for a particularly value of the tilt, but these results will be true, in general, for any value of the tilt.

5 Transport With an External Magnetic Field

In this section, we will evaluate the same Weyl system from Equation (1), but now subject to an external magnetic field. We will also shift the focus from conductivity, thermoelectric transport, and thermal transport to the Nernst effect defined in Equation (9). The reason for this shift is because the Nernst effect is a more experimentally accessible response. Furthermore, Section 4 served to illustrate the subtleties and nuances that went into individual parts of the transport. However, now that we have shown Equation (1) produces key signatures as functions of tilt and temperature, we can expand this to the Nernst effect. The same parameter values as in the previous two sections will be kept. The magnetic field will be applied in the $\hat{z}$-direction, which is on the same axis as the Weyl node separation.

5.1 Nernst Effect for a Variety of Scattering Times

In the beginning of this section, we will first consider the Nernst effect as functions of both temperature and magnetic field strength in Figure 11. The scattering time parameter, τ, will be iterated over several values. As τ increases, the Nernst effect as a function of temperature enhances in Figure 11(a-c). Additionally, the peaks in the Nernst effect generally shift up and away from $T = 0$. This shift toward positive temperatures with increasing τ is due to the c_x in the $(c_x - D)$ terms in Equations (17 - 20). In Equation (13) and Equation (14) for large values of τ, c_x and c_y both go as $\sim \tau$ with additional terms. The result is that the integrands involving $(c_x - D)$ will see an increase in c_x while D remains the same, leading to a positive shift in the integrands. The increase in peak can be explained by the scattering times multiplying the entirety of Equations (17 to 20). The transport equations all have a τ outside of their integrals so that as τ increases, so does the overall magnitude of the transport coefficients. However, the Nernst effect, from Equation (9) relies on L_{xy}^{ET} and L_{xx}^{ET} in the numerator, goes as $\sim 1/T$. The result is that the thermoelectric contributions are most prominent when temperature is lower and tapers off with higher temperatures. Thus, any contribution to the peak Nernst effect will show up at lower temperatures and allow for an increase in its maximum value and temperature location at c_x and c_y with increasing τ. Physically, Equation (12) indicates as scattering increases, the right hand side $(\frac{f-f_0}{\tau})$ must increase its difference between f and f_0. The effect is that increasing τ also separates f from f_0 more. Hence, as f increases with temperature, so too should all the transport coefficients, including the Nernst effect.

We now examine the Nernst effect as a function of field strength for various scattering times, shown in Figure 11(d-f). There are two distinct regions. One is in the low scattering limit, where the Nernst effect curves are close to linear; the other is the high scattering limit, where the Nernst effect curve approaches a anti-symmetric function. It is important to note that the function only appears antisymmetric but there is actually a small offset that preserves asymmetry. Additionally, the tilt parameter contributes to deviations from antisymmetry. Since the time reversal symmetry is broken in the Hamiltonian model, this offset from pure antisymmetry must always remain. This bears experimental ramifications, as experimental data that might initially appear antisymmetric at larger scattering times might not actually be. In the search of experimental evidence of topological time reversal breaking Weyl semimetals by Nernst measurements, this detail might avoid misinterpretations of the data.

In Figure 11, we see as we increase the Fermi energy, ϵ_F, from left to right on the plot, that plot shapes are mostly unchanging. The main exception is the scaling of Figure 11(d-f), which compresses and shifts downward. However, the exception to this general trend is $\tau = 10\frac{\hbar}{t}$, which migrates toward $-\alpha_{xyz}$. Since expressions in f_0 go as $\frac{\epsilon-\mu}{k_B T}$ and since $\mu(T)$ will generally experience an upward shift as ϵ_F increases as

shown in Figure 9(i-l), then it follows that as $\mu(T)$ increases by way of ϵ_F, then f_0 will broaden and shift with temperature. Since f_0 is spreading out over a broader range of T, then $\frac{f-f_0}{\tau}$ from Equation (12) will be more sensitive at a greater range of temperatures to $\mu(T)$. The result of this sensitivity is a change in ϵ_F generates a change in the Nernst effect for small τ values.

5.2 Nernst Effect for a Variety of Temperatures and Magnetic Fields

The plot of the Nernst effect as a function of the temperature for a variety of magnetic fields is now evaluated in Figure 12(a-c). The strength of the chemical potential crossing the nodal energy with temperature is still an important influence when considering these equations with temperature. However, there is now additional terms that go as $\frac{\epsilon-\mu}{k_B T}$ in the thermoelectric transport coefficients. Since c_x and c_y from Equations (13) and (14) depend on B by roughly $\sim B$. For $|B|$, the magnitude of the nonanomalous parts of Equations $(15-18)$ will tend to enhance, overall. However, the thermoelectric transport coefficients are different from the conductivity coefficients by $\frac{\epsilon-\mu}{k_B T}$. So, as temperature changes in the Nernst effect, the modulated magnetic field with most impacted term is L^{ET}. As temperature increases, the effects of the Fermi distribution's temperature dependence start to wash out the $\frac{\epsilon-\mu}{k_B T}$. The result yields peaks that shift for varying magnetic field in the Nernst effect.

Additionally, as the scattering time goes from a low value (Figure 12(a)), to a medium value (Figure 12(b)), and a high value (Figure 12(c)), we see that the scattering time impacts the expression of anomalous transport. The nearly symmetric Nernst curves around $\alpha_{xyz} = 0$ in the medium and high scattering regimes show that any asymmetric contribution from the anomalous terms in the transport is washed out. Higher τ values deemphasize the role of anomalous transport in the Nernst effect. A slight bump from $\alpha_{xyz} = 0$ at $B = 0$ is barely expressed in 12(b) to signify the barely noticeable anomalous effect. On the other hand, at low scattering values in Figure 12(a), the anomalous contribution is apparent, with distinguishable asymmetries and a nonzero α_{xyz} at $B = 0$ that is similarly scaled to the other nonzero B strengths.

We contemplate now the Nernst effect as a function of the magnetic field strength for a diversity of temperatures in Figure 12(d-f). This shape, similar to the Nernst effect as a function of B in Figure 11(d-f), appears antisymmetric for larger values of τ and temperatures away from $T = 0$. Terms involving D and B relate the dependence here. At smaller temperatures, the f_0 function from the Boltzmann Equation in Equation (12) approaches 1 or 0 depending on ϵ, which influences how f changes with the magnetic field. Since the nonequilibrium distribution satisfies $0 \leq f \leq 1$, then the left hand side of Equation 12 will balance this maximal difference between f and f_0 as f_0 is extremal. The result of this is that f becomes more sensitive to the magnetic field. At low temperatures, the anomalous terms will become prominent, since

they reach a maximum value as a function of temperature and settle toward 0 contribution like in Figure 10(d-f), leading to curves like the blue functions in Figure 12(d-f).

Similar to the Nernst effect as a function of the temperature in Figure 12(a-c), the Nernst curves in Figure 12(d-f) approach antisymmetry for larger scattering times and large values of temperature. Interestingly, the deviation from symmetry still exists for smaller temperatures in each of the light blue curves in Figure 12(d-f). We also notice that as the temperature increases, the Nernst curves approach close to $\alpha_{xyz} = 0$ and then rebound away. This matches the temperature dependence reaching a minimum effect and then increasing.

6 Conclusion

We started by demonstrating the differences between the free electron and a Weyl electron, mainly in regards to Bloch oscillations. We then expanded on this difference by showing how Berry curvature emulates the behavior of a magnetic field, which leads to transverse transport without applying a magnetic field. We have shown that tilt plays an important role when considering transverse anomalous transport from the Hall conductivity, the thermoelectric conductivity, and the thermal conductivity. Especially with $L^{ET}_{xy,\text{ anomalous}}$, the tilt between Lifshitz transitions most strongly interacts with the Berry curvature. We have also shown that these anomalous transport coefficients' dependence with temperature is impacted by its chemical potential crossing the Weyl nodal energy. However, each anomalous coefficient has its own sensitivity to the chemical potential based on the integration kernels f_0, s_k, and g_k belonging to $L^{EE}_{xy,\text{ anomalous}}$, $L^{ET}_{xy,\text{ anomalous}}$, and $L^{TT}_{xy,\text{ anomalous}}$ respectively. These anomalous characteristics received further investigation with the Nernst effect. Under the role of changing scattering times, we found the anomalous influences, as functions of field strength and temperature, were strongest at lower values of the scattering time. Additionally, we found the anomalous effects were also strongest for lower values of temperature. Finally, we demonstrated the Fermi energy decreases the magnitude of the Nernst effect both as a function of the field strength and temperature.

References

1. H. Weyl, *Proceedings of the National Academy of Sciences of the United States of America* **15**, 323–334, ISSN: 0027-8424 (1929).
2. B. Yan, C. Felser, *Ann. Rev. Cond. Mat. Phys.* **8**, 337 (2017).
3. M. Z. Hasan, S.-Y. Xu, I. Belopolski, C.-M. Huang, *Ann. Rev. Cond. Mat. Phys.* **8**, 289 (2017).

4. N. P. Armitage, E. J. Mele, A. Vishwanath, 2017, eprint: arXiv:1705.01111.

5. M. O. Goerbig, J.-N. Fuchs, G. Montambaux, F. Piéchon, *Phys. Rev. B* **78**, 045415 (2008).

6. A. A. Soluyanov, D. Gresch, Z. Wang, Q. Q.-S. Wu, M. Troyer, X. Dai, B. A. Bernevig, *Nature* **527**, 495 (2015).

7. Z. Wang, D. Gresch, A. A. Soluyanov, W. Xie, S. Kushwaha, X. Dai, M. Troyer, R. J. Cava, B. A. Bernevig, *Phys. Rev. Lett.* **117**, 56805 (2016).

8. Y. Sun, S. C. Wu, M. N. Ali, C. Felser, B. Yan, *Phys. Rev. B* **92**, 161107 (2015).

9. F. Y. Bruno, A. Tamai, Q. S. Wu, I. Cucchi, C. Barreteau, A. De La Torre, S. McKeown Walker, S. Ricci, Z. Wang, T. K. Kim, M. Hoesch, M. Shi, N. C. Plumb, E. Giannini, A. A. Soluyanov, F. Baumberger, *Phys. Rev. B* **94**, 121112 (2016).

10. L. Huang, T. M. McCormick, M. Ochi, Z. Zhao, M.-T. Suzuki, R. Arita, Y. Wu, D. Mou, H. Cao, J. Yan, N. Trivedi, A. Kaminski, *Nat Mater* **15**, 1155 (2016).

11. Y. Wu, D. Mou, N. H. Jo, K. Sun, L. Huang, S. L. Bud'Ko, P. C. Canfield, A. Kaminski, *Phys. Rev. B* **94**, 121113 (2016).

12. C. Wang, Y. Zhang, J. Huang, S. Nie, G. Liu, A. Liang, Y. Zhang, B. Shen, J. Liu, C. Hu, Y. Ding, D. Liu, Y. Hu, S. He, L. Zhao, L. Yu, J. Hu, J. Wei, Z. Mao, Y. Shi, X. Jia, F. Zhang, S. Zhang, F. Yang, Z. Wang, Q. Peng, H. Weng, X. Dai, Z. Fang, Z. Xu, C. Chen, X. J. Zhou, *Phys. Rev. B*, 241119 (2016).

13. L. x. Yang, Z. K. Liu, Y. Sun, H. Peng, H. F. Yang, T. Zhang, B. Zhou, Y. Zhang, Y. F. Gou, M. Rahn, D. Prabhakaran, Z. Hussain, S. K. Mo, C. Felser, B. Yan, Y. L. Chen, *Nature* **11**, 728–732 (2015).

14. J. Jiang, Z. K. Liu, Y. Sun, C. J. Rajamathi, J. P. Qi, L. X. Yang, C. Chen, H. Peng, C.-C. Hwang, S. Z. Sun, S. K. Mo, I. Vobornik, J. Fujii, S. S. P. Parkin, C. Felser, B. H. Yan, Y. L. Chen, *Nature Communications* **8**, 13973 (2017).

15. Y.-Y. Lv, X. Li, B.-B. Zhang, W. Y. Deng, S.-H. Yao, Y. B. Chen, J. Zhou, S.-T. Zhang, M.-H. Lu, L. Zhang, M. Tian, L. Sheng, Y.-F. Chen, *Phys. Rev. Lett.* **118**, 096603 (2017).

16. J. Gooth, F. Menges, C. Shekhar, V. Süß, N. Kumar, Y. Sun, U. Drechsler, R. Zierold, C. Felser, B. Gotsmann, 2017, eprint: arXiv:1706.05925.

17. S. Nakatsuji, N. Kiyohara, T. Higo, *Nature* **527**, 212 (2015).

18. N. Kiyohara, T. Tomita, S. Nakatsuji, *Phys. Rev. Applied* **5**, 064009 (2016).

19. A. K. Nayak, J. E. Fischer, Y. Sun, B. Yan, J. Karel, A. C. Komarek, C. Shekhar, N. Kumar, W. Schnelle, J. Kübler, C. Felser, S. S. P. Parkin, *Science Advances* **2**, 1501870 (2016).

20. A. Arjona, M. A. H. Vozmediano, eprint: `arXiv:1606.08318v6` (2017).

21. T. M. McCormick, R. C. McKay, N. Trivedi, *Phys. Rev. B* **96**, 235116 (2017).

22. T. M. McCormick, I. Kimchi, N. Trivedi, *Phys. Rev. B* **95**, 075133 (2017).

23. X. Wan, A. M. Turner, A. Vishwanath, S. Y. Savrasov, *Phys. Rev. B* **83**, 205101 (20 May 2011).

24. A. Bernevig, T. L. Hughes, *Topological Insulators and Topological Superconductors* (Princeton, 2013).

25. H. M. Price, T. Ozawa, N. R. Cooper, I. Carusotto, eprint: `arXiv:1412.3638v2` (2017).

26. G. Sharma, P. Goswami, S. Tewari, *Phys. Rev. B* **93**, 035116 (3 2016).

27. K.-S. Kim, H.-J. Kim, M. Sasaki, *Phys. Rev. B* **89**, 195137 (2014).

28. D. T. Son, B. Z. Spivak, *Phys. Rev. B* **88**, 104412 (2013).

29. P. Goswami, J. H. Pixley, S. Das Sarma, *Phys. Rev. B* **92**, 75205 (2015).

30. E. V. Gorbar, V. A. Miransky, I. A. Shovkovy, *Phys. Rev. B* **89**, 85126 (2014).

31. C.-L. Zhang, S.-Y. Xu, I. Belopolski, Z. Yuan, Z. Lin, B. Tong, G. Bian, N. Alidoust, C.-C. Lee, S.-M. Huang, T.-R. Chang, G. Chang, C.-H. Hsu, H.-T. Jeng, M. Neupane, D. S. Sanchez, H. Zheng, J. Wang, H. Lin, C. Zhang, H.-Z. Lu, S.-Q. Shen, T. Neupert, M. Zahid Hasan, S. Jia, *Nature Communications* **7**, 10735 (2016).

32. X. Huang, L. Zhao, Y. Long, P. Wang, D. Chen, Z. Yang, H. Liang, M. Xue, H. Weng, Z. Fang, X. Dai, G. Chen, *Phys. Rev. X* **5**, 31023 (2015).

33. M. Hirschberger, S. Kushwaha, Z. Wang, Q. Gibson, S. Liang, C. A. Belvin, B. A. Bernevig, R. J. Cava, N. P. Ong, *Nat Mater* **15**, 1161 (2016).

34. T. C. Harman, J. M. Honig, *Thermoelectric and Thermomagnetic Effects and Applications* (Macgraw-Hill, New York, 1967).

35. X. A. Zu, N. P. Ong, Y. Wang, T. Kakeshita, S. Uchida, *Nature* **406**, 486–488 (2000).

36. S. Watzman, T. M. McCormick, C. Sekhar, S.-C. Wu, Y. Sun, A. Prakash, C. Felser, N. Trivedi, J. P. Heremans, 2017, eprint: `arXiv:1703.04700`.

37. N. Ashcroft, N. Mermin, *Saunder College, Philadelphia* (1976).

38. D. Xiao, Y. Yao, Z. Fang, Q. Niu, *Phys. Rev. Lett.* **97**, 026603 (2 July 2006).

39. T. Qin, Q. Niu, J. Shi, *Phys. Rev. Lett.* **107**, 236601 (2011).

40. R. Lundgren, P. Laurell, G. A. Fiete, *Phys. Rev. B* **90**, 165115 (16 2014).

41. Q. Chen, G. A. Fiete, *Phys. Rev. B* **93**, 155125 (2016).

42. R. B. Lauer, *J. Appl. Phys.* **45**, 1794 (1974).

43. G. Sharma, C. Moore, S. Tewari, 2016, eprint: `arXiv:1605.00299`.

44. D. L. Bergman, V. Oganesyan, *Phys. Rev. Lett.* **104**, 066601 (2010).

45. N. Nagaosa, J. Sinova, S. Onoda, A. H. MacDonald, N. P. Ong, *Rev. Mod. Phys.* **82**, 1539 (2010).

46. S. J. Watzman, R. A. Duine, Y. Tserkovnyak, S. R. Boona, H. Jin, A. Prakash, Y. Zheng, J. P. Heremans, *Phys. Rev. B* **94**, 144407 (2016).

47. G. E. Volovik, eprint: `arXiv:1606.08318v6` (2016).

48. Y. Wu, N. H. Jo, M. Ochi, L. Huang, D. Mou, S. L. Bud'ko, P. C. Canfield, N. Trivedi, R. Arita, A. Kaminski, *Phys. Rev. Lett.* **115**, 166602 (16 Oct. 2015).

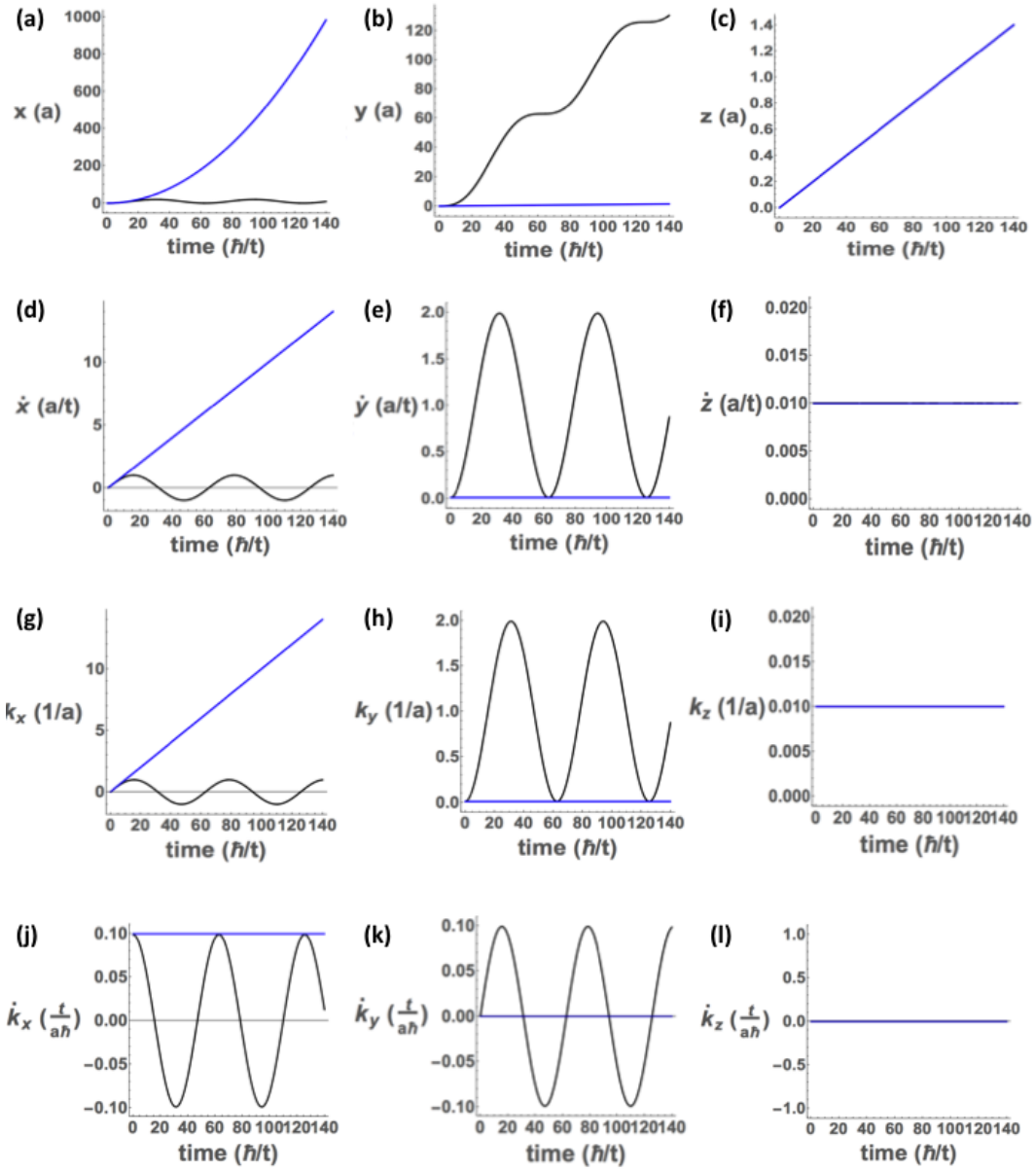

Figure 4: The blue shows the trajectories of the free electron in just an electric field while the black shows the trajectories for the free electron in an electric and magnetic field. Equations (4) and (5) were used to solve these equations. The electric field was taken in the $\hat{x}$-direction with magnitude $0.1t/(ae)$ while the magnetic field was taken in the $\hat{z}$-direction with magnitude $0.1\hbar/(ea^2)$. The initial conditions are coordinates $(0,0,0)$ in real space and $(0.01a^{-1}, 0.01a^{-1}, 0.01a^{-1})$. The left columns are in the $\hat{x}$, $\hat{k}_x$ directions, the middle column in the $\hat{y}$, $\hat{k}_y$ directions, and the right columns in the $\hat{z}$, $\hat{k}_z$ directions. (a-c) gives the spatial trajectories and (c-f) gives its time derivative, $\frac{\partial \mathbf{r}}{\partial t}$. The trajectories in momentum space are shown in (g-i) and their time derivatives, $\frac{\partial \mathbf{r}}{\partial t}$, are displayed in (j-l).

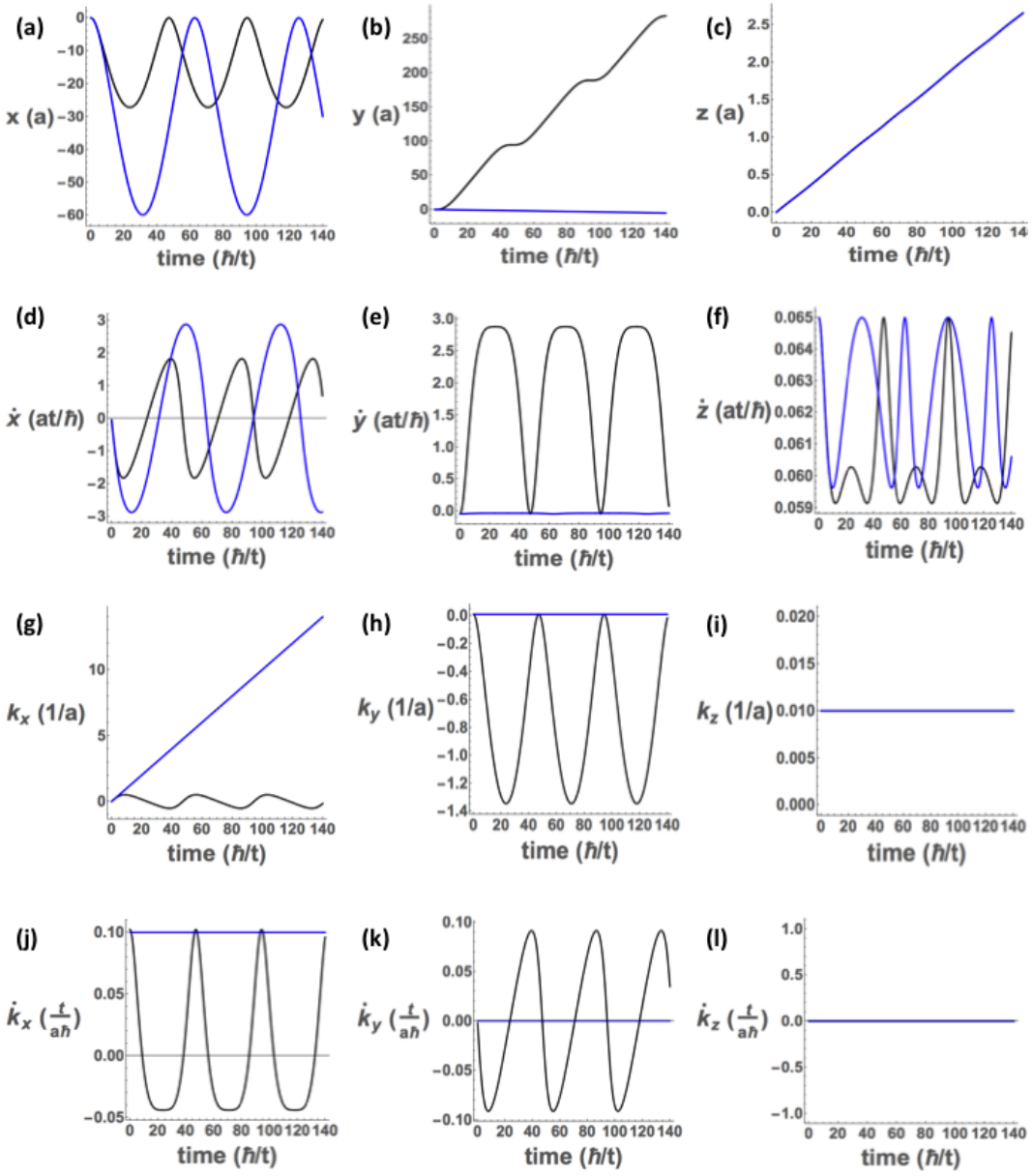

Figure 5: The type-I model from Equation 1 was used to solve the Weyl fermion's equations of motion. The blue shows the trajectories with just an electric field while the black shows the trajectories with both an electric and magnetic field. The electric field was taken in the $\hat{x}$-direction with magnitude $0.1t/(ae)$ while the magnetic field was taken in the $\hat{z}$-direction with magnitude $0.05\hbar/(ea^2)$. The initial conditions are coordinates $(0, 0, 0)$ in real space and $(0.01a^{-1}, 0.01a^{-1}, 0.01a^{-1})$ The left columns are in the $\hat{x}$, $\hat{k}_x$ directions, the middle column in the $\hat{y}$, $\hat{k}_y$ directions, and the right columns in the $\hat{z}$, $\hat{k}_z$ directions. (a-c) gives the spatial trajectories and (c-f) gives its time derivative, $\frac{\partial \mathbf{r}}{\partial t}$. The trajectories in momentum space are shown in (g-i) and their time derivatives, $\frac{\partial \mathbf{r}}{\partial t}$, are displayed in (j-l).

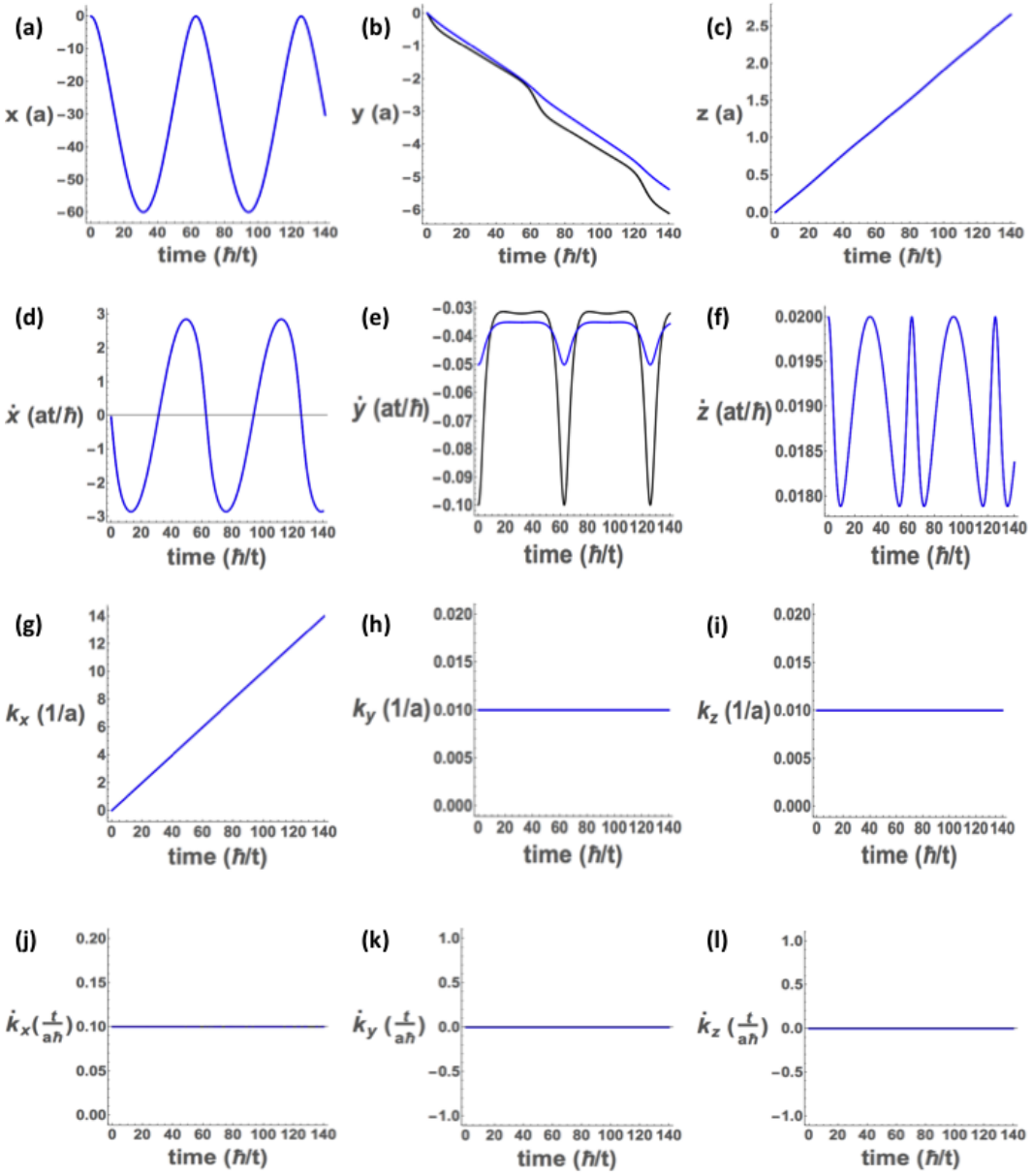

Figure 6: The type-I model from Equation 1 was used to solve the Weyl fermion's equations of motion. The blue shows the trajectories with just an electric field while the black shows the trajectories with both an electric and Berry field. he electric field was taken in the $\hat{x}$-direction with magnitude $0.1t/(ae)$ while the Berry field was derived by Equation 6. The initial conditions are coordinates $(0, 0, 0)$ in real space and $(0.01a^{-1}, 0.01a^{-1}, 0.01a^{-1})$. The left columns are in the $\hat{x}$, $\hat{k}_x$ directions, the middle column in the $\hat{y}$, $\hat{k}_y$ directions, and the right columns in the $\hat{z}$, $\hat{k}_z$ directions. (a-c) gives the spatial trajectories and (c-f) gives its time derivative, $\frac{\partial \mathbf{r}}{\partial t}$. The trajectories in momentum space are shown in (g-i) and their time derivatives, $\frac{\partial \mathbf{r}}{\partial t}$, are displayed in (j-l).

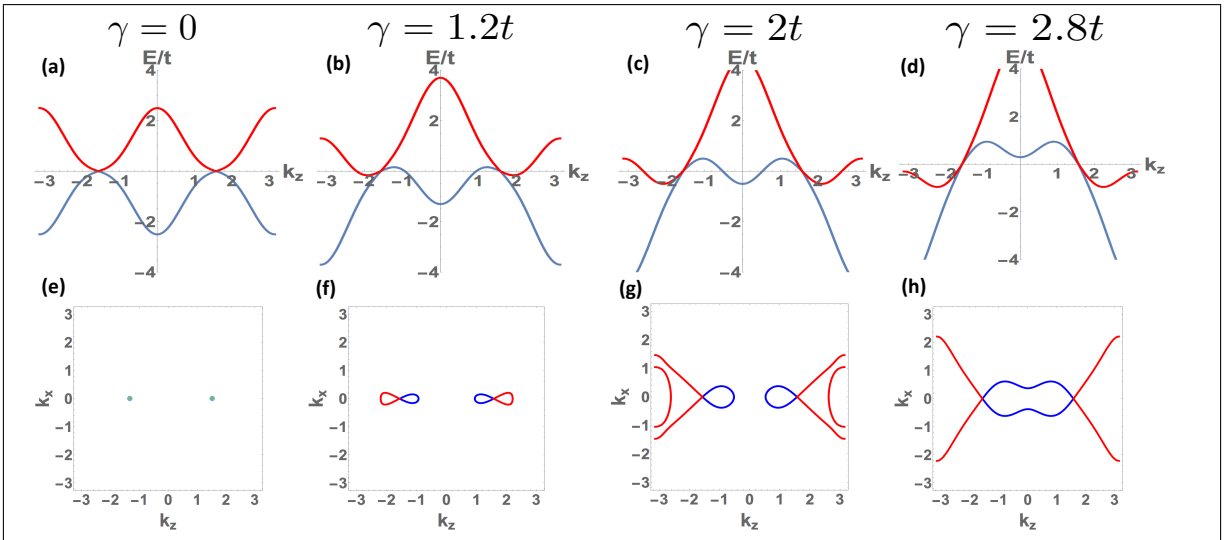

Figure 7: Cuts through the band structure given by the Hamiltonian in Equation (1). In (a-d), we show energy versus k_z cuts for $k_x = k_y = 0$. Here we have chosen $m = 3t$; $t_z = t$; $k_0 a = \pi/2$; $\gamma_z = 0.5t$ for $\gamma = 0$ (a), $\gamma = 1.2t$ (b), $\gamma = 2t$ (c), and $\gamma = 2.8t$ (d). In (e-h), constant energy cuts are shown for the band structure defined by Equation (1). (a) and (e) are in the type-I limit; (b) and (f) are in the type-II limit with distinct pockets making up each nodes; (c) and (g) are in the type-II limit after the electron pockets have merged; and (d) and (h) are in the type-II regime where the Weyl nodes share only a single electron and single hole pocket. Thus, as γ is increased the successive Lifshitz transitions described in the text emerge.

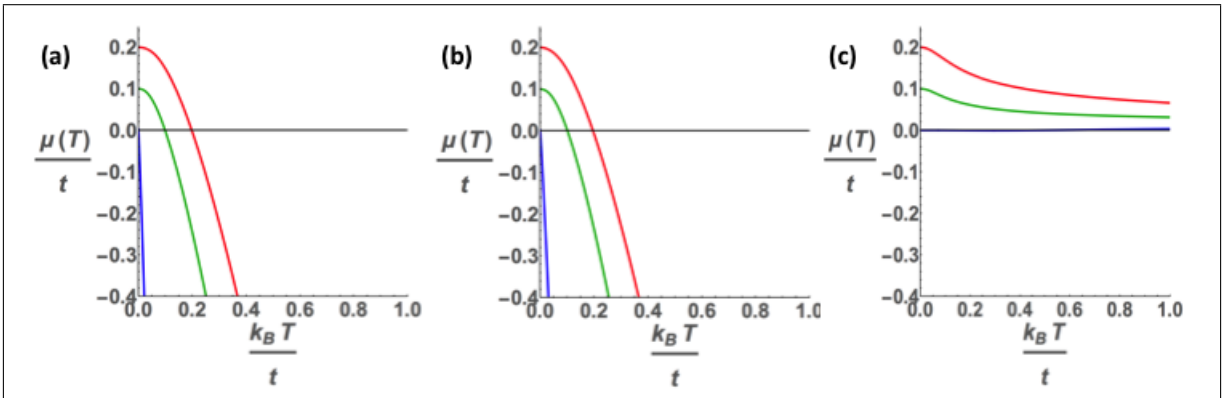

Figure 8: These show the chemical potentials changing for various lattice systems. Each of these chemical potentials is plotted for various Fermi energies, including $\epsilon_F \sim 0$ (blue), $\epsilon_F = 0.1t$ (green), and $\epsilon_F = 0.2t$ (red). The (a) plot is that of the of a quadratic energy dispersion, $\epsilon = \frac{\hbar^2 k^2}{2m}$. The (b) plot is that of a cubic lattice spacing with a single energy dispersion band of $\epsilon = -2t(\cos(k_x a) + \cos(k_y a) + \cos(k_z a)) + 6t$. The constant in the energy term is to modify how the band crosses the $\epsilon = 0$ energy. The final plot (c) shows the double band cosine dispersion, $\epsilon = \pm(-2t(\cos(k_x a) + \cos(k_y a) + \cos(k_z a)) + 6t)$.

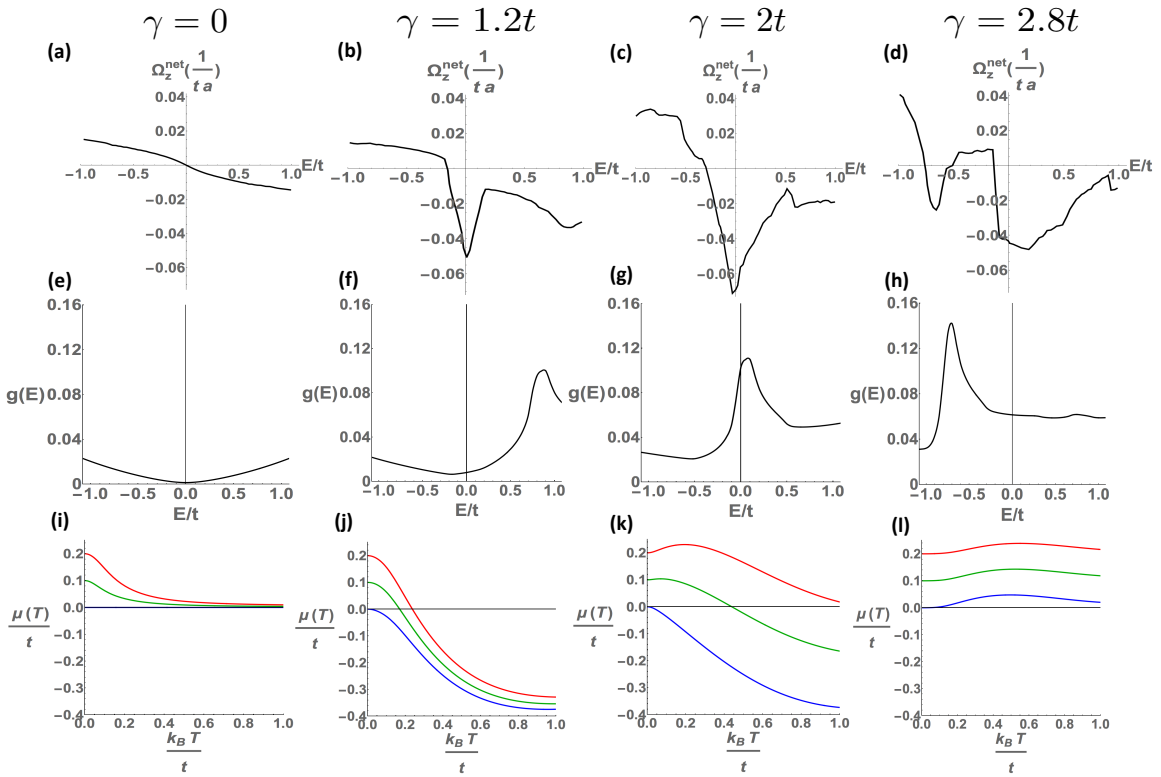

Figure 9: Each column corresponds to a particular γ with: $\gamma = 0$ (a, e, i), $\gamma = 1.2t$ (b, f, j), $\gamma = 2t$ (c, g, k), and $\gamma = 2.8t$ (d, h, l). (a-d) show the net Berry curvature in the $\hat{z}$-direction $\Omega_z^{\text{net}}(\mathcal{E})$ defined by Equation (28). For nonzero γ, the net Berry curvature around the nodes is of the same sign. (e-h) the density of states for $m = 3t$, $t_z = t$, $k_0 a = \pi/2$, and $\gamma_z = 0.5t$, for different values of the tilt parameter. (i-l) illustrates the temperature dependence of the chemical potential, $\mu(T)$. Each plot shows three separate values of ϵ_F: $\epsilon_F = 0$ (blue), $\epsilon_F = 0.1$ (green), and $\epsilon_F = 0.2$ (red). For smaller values of γ, $g(E)$ has a minimum close to the Weyl energy $E = 0$, but for larger values of γ, this minimum shifts far from the nodes. This has a strong effect on the shift of the chemical potential with temperature.

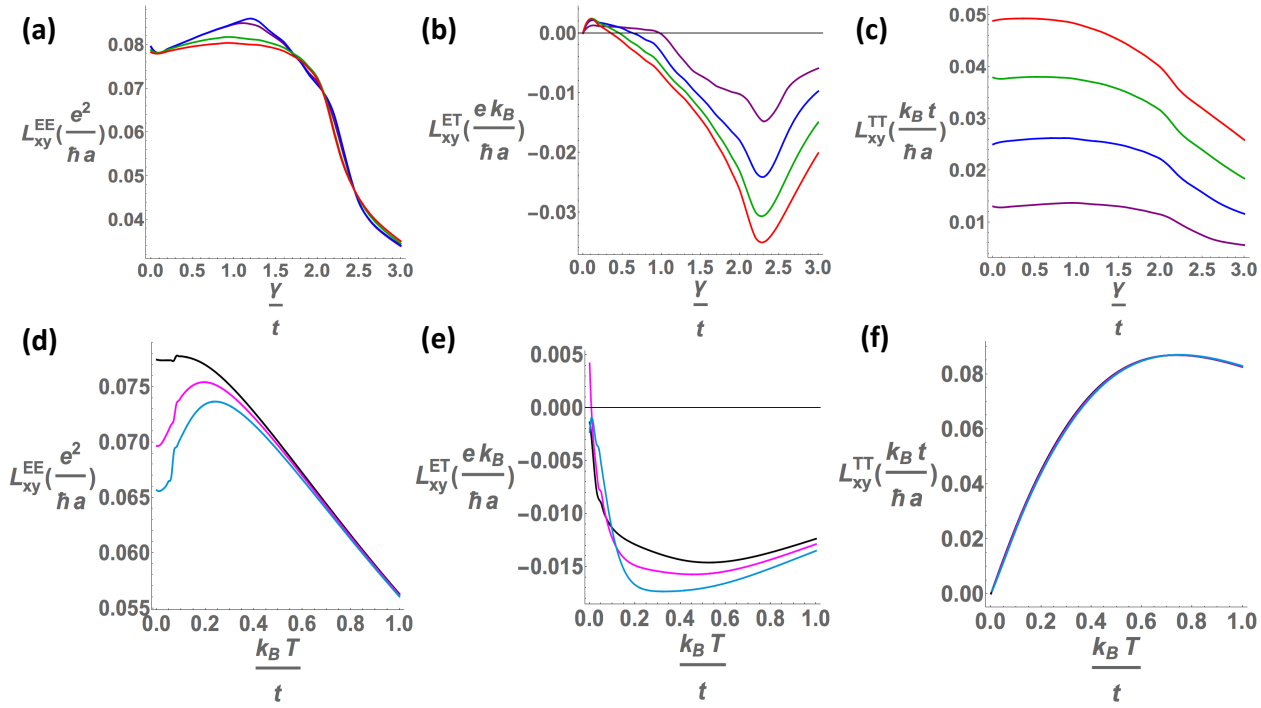

Figure 10: In (a-c), we have plotted each anomalous transport coefficient $L^{EE}_{xy,\text{ anomalous}}$, $L^{ET}_{xy,\text{ anomalous}}$, and $L^{TT}_{xy,\text{ anomalous}}$ for the Hamiltonian given by Equation (1) with parameters $m = 3t$, $t_z = t$, $k_0 a = \pi/2$, and $\gamma = 0.5t$, as a function of γ for the following temperatures: $T = 0.05t$ (purple), $T = 0.1t$ (blue), $T = 0.15t$ (green), and $T = 0.2t$ (red). In (d-f), L^{EE}_{xy}, L^{ET}_{xy}, and L^{TT}_{xy} is shown for the same values as in (a)-(c), with $\gamma = 1.2t$, plotted as functions of temperature for various Fermi energies: $\epsilon_F = 0$ (black), $\epsilon_F = 0.1t$ (magenta), and $\epsilon_F = 0.2t$ (blue).

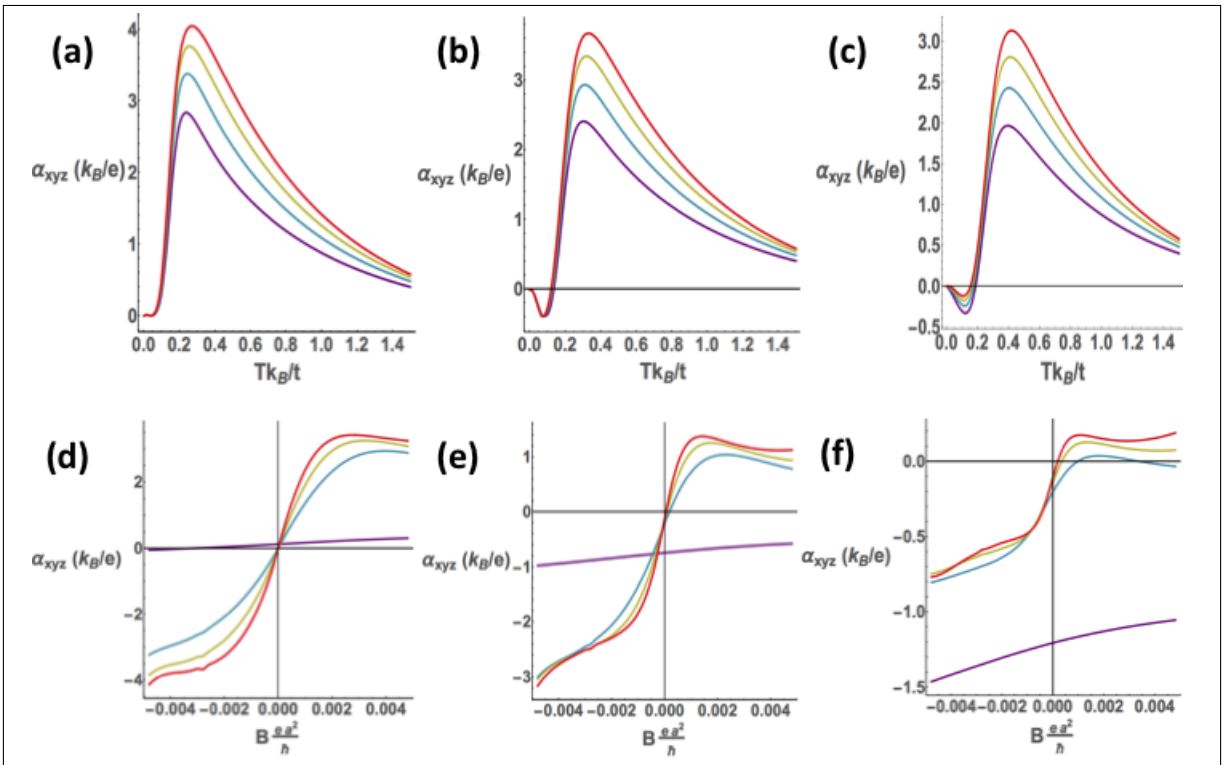

Figure 11: Plotted here is the Nernst effect as a function of temperature and magnetic field for parameters $m = 3t$, $t_z = t$, and $k_0 a = \pi/2$ in the Hamiltonian from Equation (1). In plots (a-c), where the Nernst effect is a function of temperature at $\gamma = 0$ and $B = 0.015\frac{ea^2}{\hbar}$, a diversity of τ's were chosen such that $\tau = 150\hbar/t$ (purple), $\tau = 200\hbar/t$ (teal), $\tau = 250\hbar/t$ (yellow), and $\tau = 300\hbar/t$ (red). For the Nernst effect when $\gamma = 1.2t$ and $T = 0.201\frac{k_B}{t}$ as a function of the magnetic field strength in (d-f), several τ's are also represented: $\tau = 10\hbar/t$ (purple), $\tau = 100\hbar/t$ (teal), $\tau = 150\hbar/t$ (yellow), and $\tau = 200\hbar/t$ (red). Also, different Fermi energies were considered: (a) and (d) at $\epsilon_f = 0$, (b) and (e) at $\epsilon_f = 0.2t$, and (c) and (f) at $\epsilon = 0.4t$.

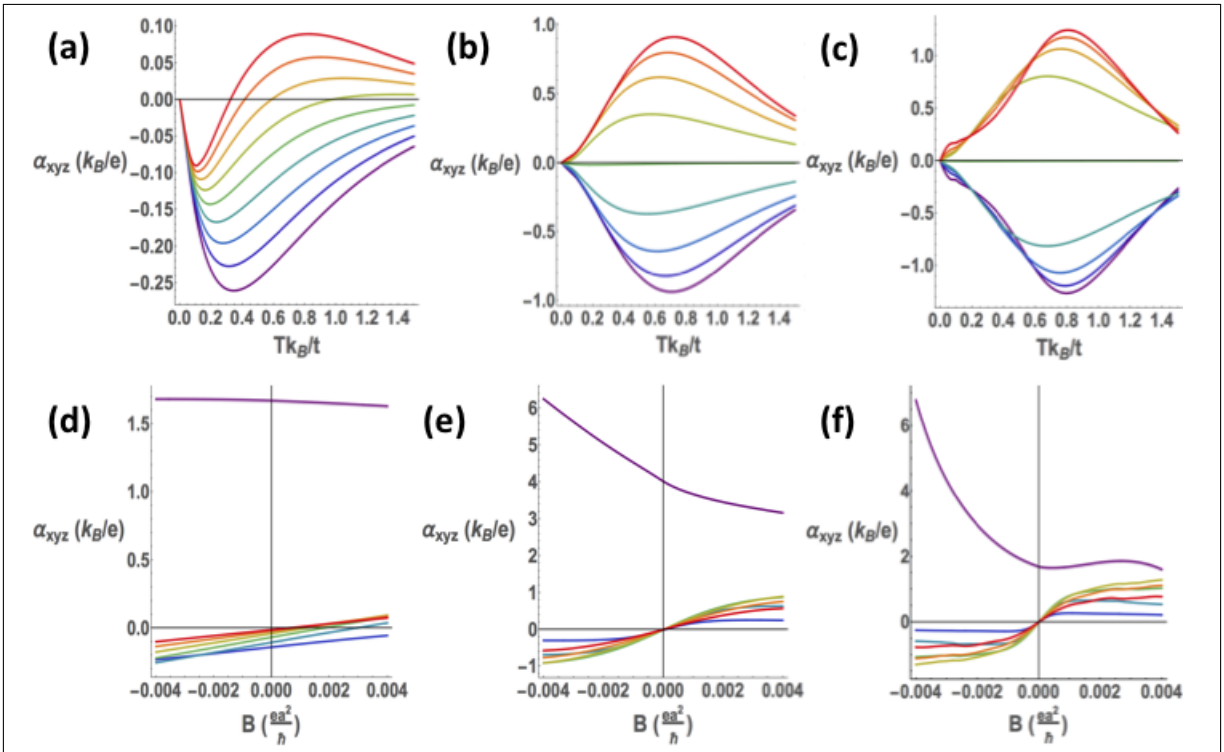

Figure 12: The Hamiltonian in Equation (1) was used with the parameters $m = 3t$, $t_z = t$, $k_0 a = \pi/2$, $\gamma = 2t$, and $\epsilon_F = 0.2t$. (a) and (d) correspond to $\tau = 10\hbar/t$, (b) and (e) correspond to $\tau = 100\hbar/t$, and (c) and (f) correspond to $\tau = 300\hbar/t$. Plotted in (a-c) is the Nernst effect, given in Equation (9), as a function of temperature. A variety of magnetic fields are plotted in each case: $B = 0.004\frac{ea^2}{\hbar}$ (red), $B = 0.003\frac{ea^2}{\hbar}$ (dark orange), $B = 0.002\frac{ea^2}{\hbar}$ (light orange), $B = 0.001\frac{ea^2}{\hbar}$ (light green), $B = 0$ (green), $B = -0.001\frac{ea^2}{\hbar}$ (teal), $B = -0.002\frac{ea^2}{\hbar}$ (blue), $B = -0.003\frac{ea^2}{\hbar}$ (dark blue), and $B = -0.004\frac{ea^2}{\hbar}$ (purple). Plots (d-f) are the Nernst effect as a function of the magnetic field strength for a variety of temperatures. The temperatures correspond to $T = 0.001k_B/t$ (purple), $T = 0.201k_B/t$ (dark blue), $T = 0.401k_B/t$ (light blue), $T = 0.601k_B/t$ (green), $T = 0.801k_B/t$ (yellow), $T = 1.001k_B/t$ (orange), and $T = 1.201k_B/t$ (red).